

Enhanced Stokes Shift and Phase Stability by Cosynthesizing Perovskite Nanoparticles (MAPbI₃/MAPbBr₃) in a Single Solution

Muhammad Munir, Jinglan Tan, Ramis Arbi, Pedro Oliveira, Elisabeth Leeb, Yolanda Salinas, Markus Clark Scharber, Niyazi Serdar Sariciftci, and Ayse Turak*

Herein, diblock copolymer reverse micelle templating (RMD) is used to control the reaction kinetics of metal halide hybrid perovskites formation to fabricate systems showing dual-phase emission. Through micelle templating, desired compositions can be engineered which show high phase stability of mixtures of perovskite nanoparticles (NPs) through micellar shielding and stabilizing of the cage structure. In addition, Stokes shift of around 150 nm, one of the largest reported for perovskite systems, can be obtained with careful control over synthesis kinetics. Using an unconventional approach, that is, mixing methylammonium iodide (MAI) and lead bromide PbBr₂, systems consisting of both green- and red-emitting NPs are fabricated by a two-step reaction process using RMD. By obtaining two stable phases in a single solution, the NP system can absorb in the ultraviolet region and emit in the red region, making them excellent candidates for downconversion to improve solar cells efficiency, as shown for two polymer active layers in organic bulk heterojunction solar cells (OPVs). Exploiting the phase stabilizing effect of the micelles, the reaction kinetics of perovskite formation can be tuned for various halide substitutions, opening up new avenues for coexisting perovskite phases for photovoltaic and light-emitting applications.

1. Introduction


In recent decades, the family of metal halide hybrid perovskites has attracted attention owing to record-breaking achievements in fields such as photovoltaics (PV), light-emitting diodes (LEDs), lasers, sensors, and many other electronic devices.^[1–7] Perovskites, with the generic chemical formula ABX₃, owe these properties to their flexible cage crystal structure where the A-site is occupied by a monovalent cation which could either be an organic molecule, such as methylammonium (CH₃NH₃⁺) (MA) or formamidinium (CH(NH₂)₂⁺) (FA), or an inorganic atom, such as cesium (Cs⁺); the B-site accommodates a divalent inorganic cation such as lead (Pb²⁺) or tin (Sn²⁺); and X position is occupied by a halide group, which could be chloride (Cl⁻), bromide (Br⁻), or iodide (I⁻).^[8]

A critical issue hindering the commercialization of perovskite-based optoelectronic devices is instability and phase degradation. The desirable α -phase perovskite structure, which is ideal for photoelectric conversion, eventually degrades in ambient conditions into the δ -phase, which is a yellowish nonperovskite phase with an unwanted large bandgap and poor charge transport.^[3,9–12] Various approaches have been attempted to limit such degradation processes. Common is to use encapsulation approaches, including copolymer micellar shielding,^[13–15] core-shell formation,^[15,16] polymer coprecipitation,^[17] solid polymer composite formation,^[18–21] incorporation into metal-organic frameworks (MOFs),^[22] or in situ stabilization in mesoporous templates.^[23] Another approach is through substitution of suitable ions which stabilize the cage symmetry of optically active perovskites.^[6,24,25] Importantly, the substitution of ions also induces changes in the emission and absorption spectrum of the parent composition, resulting in a tunable bandgap by tailoring of the ionic composition.^[26] Substitution of halides in particular can be leveraged to tune the emission maxima of the perovskite between $400 \leq \lambda \leq 800$ nm.^[27–29] Therefore, halide substitution offers the best avenue for improving the stability of ABX₃ perovskites, while simultaneously allowing bandgap tunability.

M. Munir, J. Tan, R. Arbi, P. Oliveira, A. Turak
Department of Engineering Physics
McMaster University
L8S 4L7 Hamilton, ON, Canada
E-mail: turaka@mcmaster.ca

E. Leeb, Y. Salinas
Institute of Polymer Chemistry (ICP)
Johannes Kepler University
A-4040 Linz, Austria

M. C. Scharber, N. S. Sariciftci
Linz Institute for Organic Solar Cells (LIOS)
Institute of Physical Chemistry (IPC)
Johannes Kepler University
A-4040 Linz, Austria

 The ORCID identification number(s) for the author(s) of this article can be found under <https://doi.org/10.1002/adpr.202100372>.

© 2022 The Authors. Advanced Photonics Research published by Wiley-VCH GmbH. This is an open access article under the terms of the Creative Commons Attribution License, which permits use, distribution and reproduction in any medium, provided the original work is properly cited.

DOI: 10.1002/adpr.202100372

Phase purity or achieving a desired composition can be complicated, however, by incomplete substitution and lack of control over the formation of the final product. All such substitution attempts either involve the addition of a third or fourth precursor in precise stoichiometric amounts or require extra steps after perovskite formation to incorporate the desired halides in the already formed perovskite. It can be difficult to achieve and maintain the desired synthesis, due to the very fast reaction kinetics of perovskite formation.^[30–32] Chauhan et al. monitored the absorption and emission spectra during the formation of MAPbI₃ during a two-step synthesis process, where they concluded that it took only 14 s (including the deposition time) for the precursors to form the final perovskite product.^[33] The fast reaction kinetics using conventional approaches do not typically allow for the introduction of additional ions once the reaction is started, making the precise tuning of composition very challenging. Fast halide reaction kinetics inside the perovskite cage and its phase instability leads to anionic substitution even in the absence of a parent halide source. Nedelcu et al. demonstrated that for the first 30 sec of mixing prefabricated cesium lead iodide (CsPbI₃) and cesium lead bromide (CsPbBr₃), two distinct peaks (one for iodide-based perovskite and one for bromide-based perovskite) were visible; however, with further mixing, both the peaks merged into a single peak, resulting in the formation of a single mixed-phase perovskite.^[11]

These issues are exacerbated for nanoparticle (NP) systems, where the large surface area-to-volume ratio often leads to high phase instability. However, perovskite nanostructures are highly desirable because of their high photoluminescence (PL) quantum yield at room temperature, approaching almost 100%;^[34] easy optical tunability;^[35] long PL lifetime;^[36] and a high tolerance for defects.^[3]

In this work, we have successfully controlled the reaction kinetics and slowed down the rate of perovskite formation using diblock copolymer reverse micelle templating (RMD). The slowed reaction allows the use of an unconventional approach, mixing methylammonium iodide (MAI) and lead bromide (PbBr₃) to produce pure methylammonium lead bromide MAPbBr₃ NPs. This anionic exchange was done without the engagement of any catalysts and at room temperature. This synthesis route also allows for the simultaneous formation of stable and luminescent MAPbI₃-dominant and MAPbBr₃-dominant NPs coexisting within a single solution. As our NPs are fabricated within the core of diblock copolymer micelles, they are shielded by the hydrophobic polystyrene (PS) branch of the amphiphilic diblock copolymer which forms the corona of the micelles. Phase degradation is therefore prevented by the micelle, allowing for tuning of the relative abundance of each NP within the solution. The presence of both iodine and bromine leads to a more stable, nondegradable perovskite phase because the most suitable anion occupies the available positions within the perovskite cage, limiting mixed-phase formation. The NPs are also sheltered from the external atmosphere (oxygen and humidity), owing to the shielding offered by the hydrophobic corona. These give rise to interesting properties for the NPs such as a large Stokes shift, resulting from self-trapped exciton state (STE) formation due to coexistence of two halide ions. By tuning the emission characteristics, the NPs synthesized from the same precursors with slightly different deposition conditions can be effectively used to downconvert UV light into useable

photons, enhancing the device performance of OPVs based on both poly(3-hexylthiophene) (P3HT) and poly [[4,8-bis[(2-ethylhexyl)oxy]benzo[1,2-b:4,5-b']dithiophene-2,6-diyl][3-fluoro-2-[(2-ethylhexyl)carbonyl]thieno[3,4-b]thiophenediyl]] (PTB7) bulk heterojunction blends with [6,6]-phenyl C61-butyric acid methylester (PCBM) as active layers, even though they have different absorption regions.

2. Results and Discussion

Using diblock copolymer templates, we have been able to produce various perovskite NPs using a two-step RMD process.^[13] Iodine-based perovskite synthesis was relatively straightforward utilizing MAI and PbI₂ loaded sequentially to obtain uniform, well-dispersed MAPbI₃ NPs, from PS-*b*-P2VP nanoreactors. Infiltration of MAI was found to stabilize the micelle, preventing the destructive interaction of Pb-based precursors,^[13] as shown schematically in **Figure 1a**. **Figure 1b** shows the PL emission spectrum with inset atomic force microscopy (AFM) micrograph from well-dispersed MAPbI₃ NPs, fabricated using the two-step loading process. However, MABr did not produce the same stabilizing effect, and upon adding PbBr₃, no NPs could be obtained, as shown in **Figure 1c**. Attempts at imaging micelles after the addition of both precursors (MABr and PbBr₃) revealed nonmicellar structures, similar to the structures observed when the lead precursor was added first to the micelle solution. This suggests that the organic ion failed to infiltrate the core; as a result, the micelle core was not stabilized and unraveled on the introduction of the lead salt due to the strong affinity between Pb and 2VP units.^[13]

Typically for NP synthesis and size control, high-molecular-weight polymers are chosen that form dense-core micelles, where the corona offers tight shielding against the environment.^[20,37,38] Using lower-molecular-weight polymers results in the formation of a larger ballooning micelle structure with a looser corona of shorter PS chains, allowing easier infiltration of precursor salts^[37] (see **Figure S1**, Supporting Information). However, the downside of such a micellar structure is lowered protection from hydration, as proven by Arbi et al., in the case of polymorphic iron oxide phase formation using different PS-*b*-P2VP diblock copolymer micelles.^[37] The failure of MABr loading in the higher-molecular-weight PS-*b*-P2VP micelles results from its failure to infiltrate the densely packed polystyrene brushes in the corona. Using lower-molecular-weight polymers led to successful synthesis of MAPbBr₃ NPs from MABr and PbBr₃ precursors; however, it also resulted in an uneven size and spatial distribution, as shown in **Figure 1d**.

Anionic substitution by adding bromide compounds to iodine-based perovskites has been previously successfully shown to convert perovskites from one phase to another.^[11,39–43] Therefore, we added MABr and PbBr₃ individually to presynthesized MAPbI₃ NP solutions. After 24 h stirring time, a slight hypsochromic shift was observed in the emission spectra of the solution, which is shown in **Figure 1e**. Both the spectra were blueshifted compared with pristine MAPbI₃ spectrum, with a maxima at 735 nm for MABr addition and at 714 nm for PbBr₃ addition. There was also a broad shoulder artifact with a peak around 550 nm, suggesting formation of some

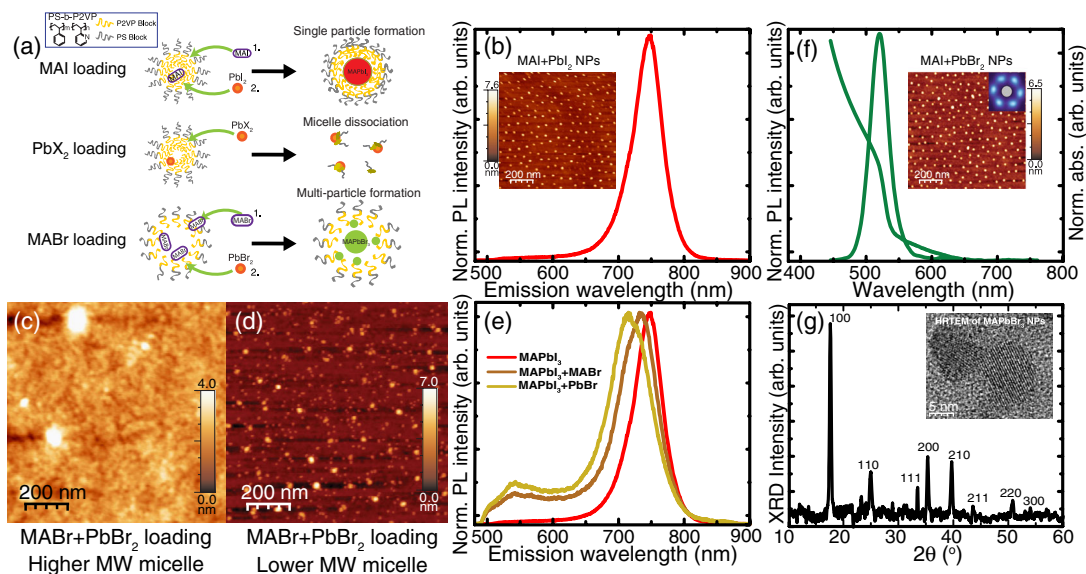


Figure 1. a) Schematic of direct synthesis of MAPbI₃/MAPbBr₃ NPs using the reverse micelle nanoreactor process. Numbers refer to the order of precursor addition, with the organic cation added 24 h prior to the halide. If there is no organic cation inside the micelle, the addition of the lead halide leads to micelle destruction and no NPs are formed. Dense crewcut micelles with high-molecular-weight polymers result in individual NPs, and large balloon-type micelles with low-molecular-weight polymers result in multiple particles forming inside the nanoreactor. b) PL emission spectrum and AFM image of MAPbI₃ NPs synthesized with conventional precursors (MAI and PbI). c) AFM image of unsuccessful attempts to synthesize MAPbBr₃ in dense-core high-molecular-weight micelles using direct synthesis route with conventional precursors. d) MAPbBr₃ NPs with wide size distribution obtained using conventional precursors (MABr and PbBr₃) in balloon-like lower-molecular-weight micelles. e) PL emission spectrum showing a bathochromic shift in presynthesized MAPbI₃ NPs after the addition of PbBr and MABr to micelle solution. f) PL emission and UV-vis absorption spectra of MAPbBr₃ NPs synthesized by unconventional route using MAI and PbBr₃ after 24 h of stirring at room temperature; the inset AFM image shows the well-ordered NP formation. The density cloud (fast Fourier transform) of the NP dispersion shows strong hexagonal packing of the NPs. g) XRD spectrum of MAPbBr₃ NPs synthesized with unconventional precursors. Inset shows HRTEM images of the nanoparticles with visible lattice fringes.

MAPbBr₃. This suggests that only fractional anionic substitution occurred inducing a slight blueshift, not forming pristine MAPbBr₃ NPs, even though the solutions were left to stir for times substantially longer than the complete conversion times observed by others.^[11,43] Complete substitution is inhibited both by the micellar shielding and by the covalent character of iodine, which is more than that of bromine; therefore, once a stable MAPbI₃ NP is formed inside a nanoreactor, all the iodine cannot be replaced fully by halide substitution.

As MAI has been shown to stabilize the PS-*P*-2VP nanoreactors, and as quaternization with iodine is known to encourage salt interaction with diblock copolymers,^[44,45] an unconventional route using mixed precursors MAI and PbBr₃ was used to synthesize MAPbBr₃ NPs, as shown in Figure 1f. PL emission and UV absorption spectrum of the NPs confirm the formation of MAPbBr₃, with an emission peak at 521 nm (full width at half maximum (FWHM) of 30.03 nm), and a bandgap of 2.28 nm, from Tauc analysis of the absorption spectra (see Figure S3, green spectrum, Supporting Information). The inset shows an AFM micrograph of the dispersion of the synthesized NPs with polydispersity index for the NP diameters of 0.096 (i.e., <10% variation in size), nearest-neighbor distance of roughly 78 nm, and a quasi-hexagonal array with lattice distortion^[46] of only 8.56 (see Figure S14, Supporting Information, for full spatial statistics). X-ray diffraction (XRD) results, shown in Figure 1g, further confirm the formation of MAPbBr₃. Peaks at 2θ of 17.4, 24.7, 31.4, 35.3, 39.65, 43.62, 50.8, and 54.1 correspond to reflection planes

100, 110, 111, 200, 210, 211, 220, and 300 of MAPbBr₃. The XRD results confirm the space group of *Pm-3m* and cubic symmetry of NPs with lattice parameter of 5.89 Å.^[47] Inset of Figure 1g also displays high resolution transmission electron microscopy (HRTEM) images of the formed MAPbBr₃ NPs. The NPs were resolved to be ≈6.1 nm.

The significant benefit of the reverse micelle route is the ability of the iodide salt to penetrate the dense-core micelles, owing to the strong interaction between the P2VP group of the micelles and the iodide ion. Iodine is well known for preferentially staining pyridine over polystyrene and has been utilized to improve contrast in electron microscopy of the diblock copolymer.^[48] The addition of the iodide stabilizes the core by quaternization with the P2VP group of the diblock copolymer, while leaving it unchanged in the presence of a more reactive ion.^[49] The infiltration of the iodine and the quaternization of the P2VP block of the diblock copolymer seem to trigger a rearrangement of the PS chains in the corona, allowing for a more feasible entry for the second added precursor, PbBr₃.

When Pb²⁺ and Br⁻ infiltrate into the core, they rearrange in the presence of MA⁺, and a very stable and highly emissive MAPbBr₃ NP is formed encapsulated by the diblock copolymer. We also saw similar behavior using other iodide precursors, such as formadimium iodide, showing the general applicability of the organometallic iodide stabilizing the core (see Figure S5, Supporting Information). The schematic of MAPbBr₃ creation inside the dense-core diblock copolymer is shown in Figure 2,

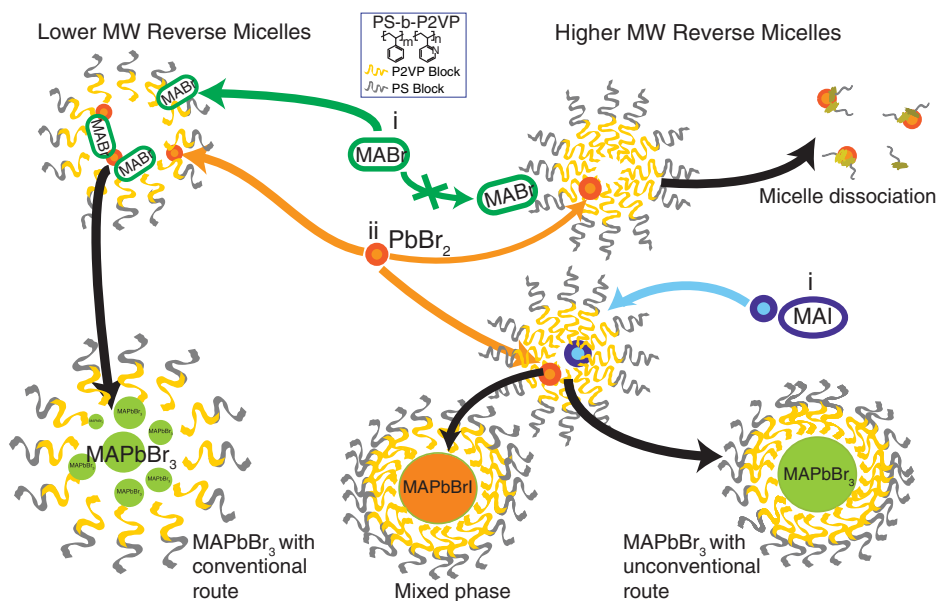


Figure 2. Schematic diagram of MAPbBr₃ fabrication utilizing anionic exchange phenomenon with both iodide and bromide precursors.

which also illustrates the unraveling of the nanoreactor by the Pb precursor alone. Interestingly despite the presence of both iodide and bromide ions, pure MAPbBr₃ NPs were formed. There are two main justifications for this preferential formation. On the one hand, the formation rate constant and stability constant for iodine–pyridine complexes are higher than that of bromine–pyridine complexes.^[49,50] Therefore, once complexed, it would not be easy to replace iodine due to the overlap of the π^* orbital of I₂ with the pyridine LUMO.^[49] This suggests that the iodine would remain complexed to the polymer preferentially over the bromine, leaving the bromine free to form the perovskite. On the other hand, the formation of MAPbBr₃ in the presence of both I⁻ and Br⁻ ions can also be justified in terms of the Gibbs free energy of formation of MAPbBr₃ and MAPbI₃. The calculated and extracted Gibbs free energy of MAPbBr₃ reported by different researchers, (−12.5, −3.5, and −17.0 kJ mol⁻¹) from MAX and PbX₂ is always lower than that for MAPbI₃ (−11.3, 22.8, and −7.2 kJ mol⁻¹), which thermodynamically validates the preferential formation of MAPbBr₃ in such a situation.^[51–53] Yet, pure-phase formation is typically not observed with mixed precursors due to the extremely fast reaction kinetics during perovskite formation, instead resulting in mixed phases.

It is well understood that metal halide hybrid perovskites form quickly once the precursors are mixed together.^[54–59] Chauhan et al. saw final perovskite formation within 14 s of adding the precursors;^[33] Nedelcu et al. showed that mixed phases form after only 30 s.^[11] Such fast reaction kinetics using conventional approaches do not allow for the introduction of additional ions once the reaction is started. To examine the mechanisms of this reaction in the presence of the micelles, time-resolved PL spectroscopy was performed and tracked over 24 h after the addition of precursors to observe the kinetics of this unconventional approach. The formation of MAPbBr₃ NPs with stirring time can be observed from **Figure 3a**, with increasing PL intensity

with time of stirring. After 2 min, we can observe conversion of the organic salt into MAPbBr₃ with sharp emission at 532 nm starting to emerge. This emission continues to sharpen with time, becoming more intense and clearly visible as a sharp peak \approx 10 min after the addition of the second precursor. A slight redshift in emission suggests that the particles are also starting to grow in size over a short time. The emission from unreacted MAI forming the background extending to beyond 750 nm is still visible after 20 min reaction time. The intensity of the emission peak steadily increased until a maximum was reached after stirring for 24 h, with no visible background emission and no further change observed. There is a slight blueshift to 526 nm after this stirring time, potentially suggesting that there may be a mixture of I/Br in the initially formed crystals, but they become more bromine dominant (more MAPbBr₃ like) after prolonged stirring.

The micellar environment is critical to the formation of these NPs, providing a stabilized environment for the reaction. To verify how MAI and PbBr₃ interact in the absence of the nanoreactors, both the precursors were added to *o*-xylene directly in the same concentration as that added to the reverse micelle solution in *o*-xylene. As soon as the second precursor was added (in milliseconds), a very broad peak of MAPbI₃ appeared and the spectrum maxima kept shifting within a range from 20 to 25 nm, as shown in **Figure 3b**. There was also significant crystallization and visible precipitation of the precursors immediately, and when the supernatant solution was characterized after 4 h, no emission spectrum could be observed. This illustrates the instability of the produced perovskite phase in the presence of *o*-xylene and bromide ions without reverse micelles, where fast reaction kinetics prevent the formation of MAPbBr₃.

This was further compared with a standard method of NP growth, ligand-assisted reprecipitation (LARP), using oleic acid and oleylamine. Unlike MABr and PbBr₃, which resulted in bright and luminescent NP films, as shown in **Figure 3c** (green spectrum), MAI and PbBr₃ showed almost no emission

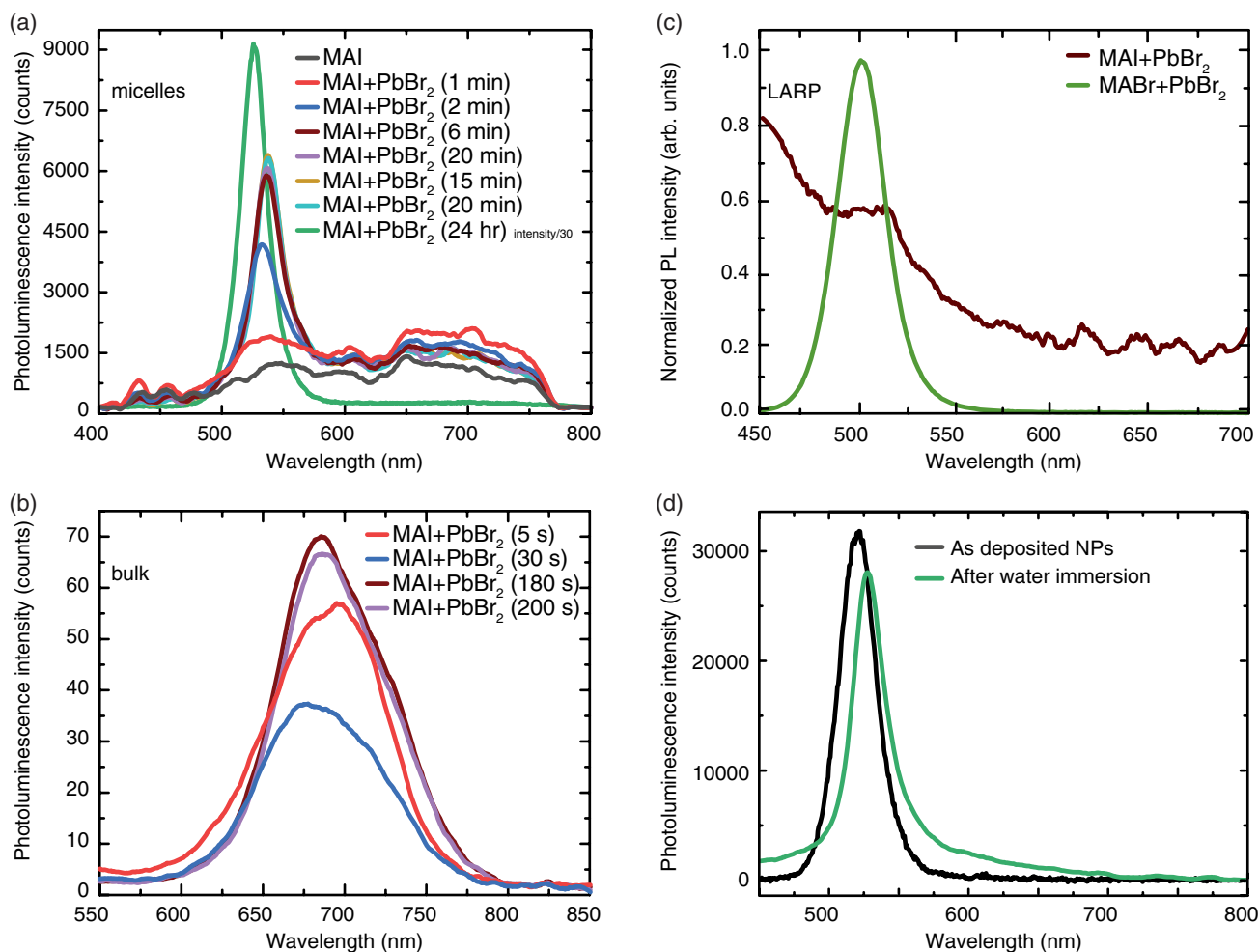


Figure 3. a) Time-resolved PL of MAPbBr₃ NPs formation through an unconventional anionic exchange route with MAI and PbBr₂ in diblock copolymer micelles. b) Time-resolved emission spectrum of MAI and PbBr₃, mixed in *o*-xylene. c) PL emission spectrum of MAPbBr₃ NPs fabricated using LARP synthesis route with conventional precursors (MAI and PbBr₃) (green) and unconventional precursors (maroon). d) PL emission spectra of NPs after (green line) and before (black line) interaction with water.

(Figure 3c (maroon spectrum)). Unlike the RMD approach, where the micelles provide a shielded nanoreactor for uniform and luminescent MAPbBr₃ NPs, in LARP, the ligands typically rapidly detach and reattach as precursor molecules encounter the forming crystal, resulting in inhomogeneous elongated crystals rather than true 0D NP.^[2,31,60,61] The slower reaction kinetics from RMD and the interaction of the iodine with the P2VP in the micelle core allow the formation of the thermodynamically stable MAPbBr₃-dominated NPs, which were suppressed in the fast reaction kinetics of ligand-assisted approaches.

The stabilizing environment provided by the micelle also enhances the stability of the NPs with exposure to other precursors or to humidity. To verify the stability of our synthesized NPs in solution, we added PbI₂ to the centrifuged solution of FAPbBr₃ NPs produced from FAI and PbBr₃ and stirred them for 24 h (see Figure S5, Supporting Information). No shift was noticed in the emission spectrum suggesting that no anionic substitution occurs with additional precursor, making the NPs more stable than conventional NPs where reversible mixed phases are formed.^[3,29,41,62]

Micellar environments are also known to increase the stability of perovskite NPs in the ambient environment.^[13,15,16,63] We also confirmed the stability of our produced NPs in the presence of moisture by letting a spin-coated sample float over water in 100% humidity for 4 h, followed by immersion in water for 10 min. The PL emission spectra before and after water immersion can be seen from Figure 3d. A slight change in the intensity of the PL emission spectrum was noticed, which could be attributed to characterization of two different spots for the pre- and post-treated sample. Strong emission despite the interaction of NPs with water validates that the micelle not only protects the NPs from the ambient atmosphere but also protects them from direct water interaction.

We can take advantage of the slower kinetics involved in this synthesis approach, as well as the presence of both bromine and iodine, to engineer the NP solution by controlling different factors throughout the synthesis process, such as the infiltration time, amount of precursors, or number of nanoreactors to achieve various novel phases.

First, we increased the concentration of nanoreactors by increasing the amount of PS-*b*-P2VP diblock copolymer

dissolved in the solvent by a factor of 4, to 12 g L^{-1} . This has been known to increase the density of particles as well as decrease the size and spacing of particles.^[64] As the concentration increases, residual solvent is excluded and the structure becomes more compact. To maintain the salt-to-P2VP ratio, we increased the amount of precursor to $10 \mu\text{L}$ of MAI and PbBr_3 to account for the increasing diblock copolymer blocks per unit volume. The loading was then performed, with a 24 h loading time

between precursor additions. By varying the polymer concentration and the precursor amount, a different PL emission spectrum emerged dominated by MAPbBr_3 , as expected, but with some intensity suggestive of MAPbI_3 centered at 725 nm , as shown in **Figure 4a** (brown spectrum). The Tauc plot derived from the UV absorption data (see Figure S3, Supporting Information, brown spectrum) indicates a slight decrease in the bandgap of the bromide-dominant NPs. As expected with

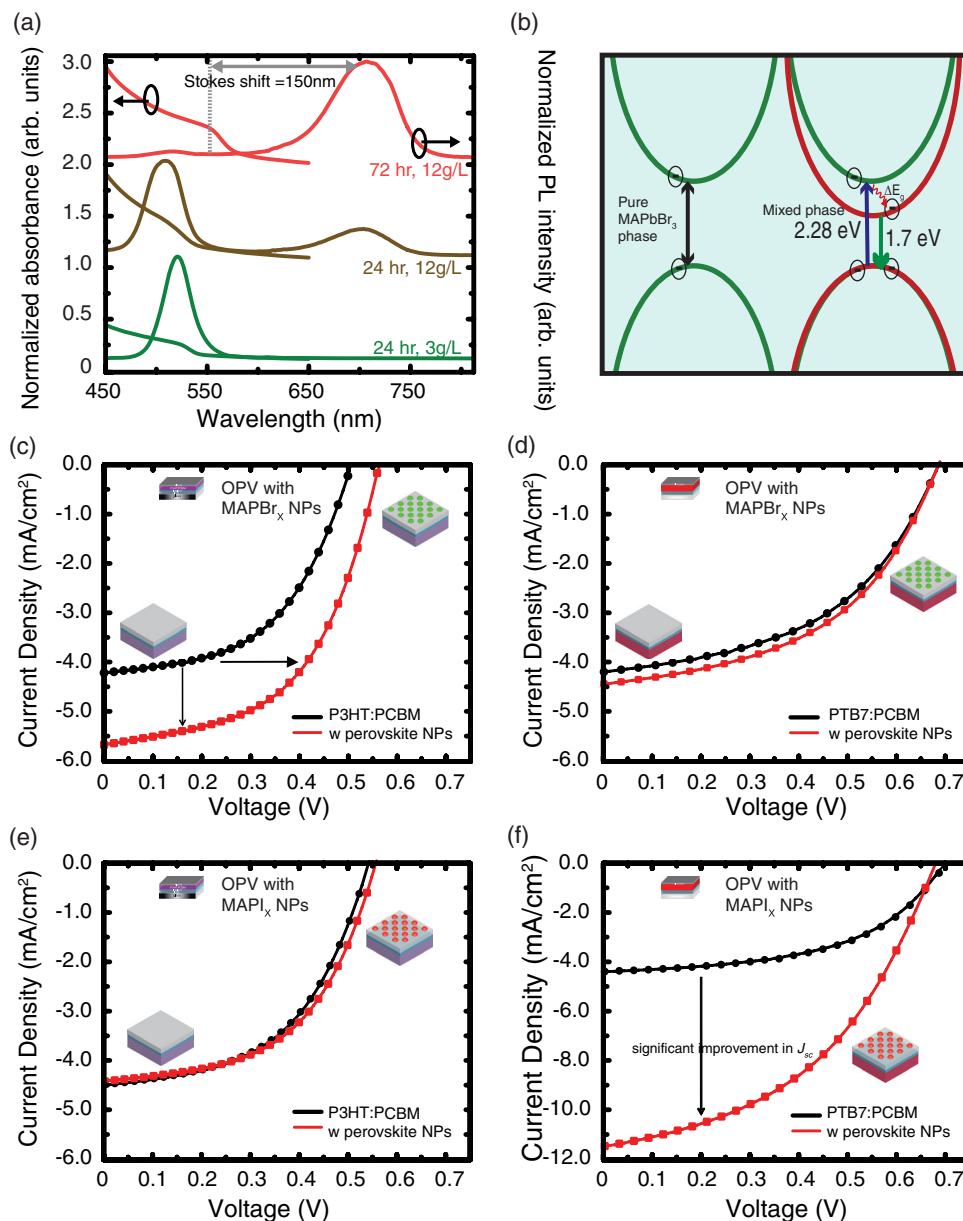


Figure 4. a) UV-vis absorption and PL emission spectrum of solutions for MAPbBr_3 with 24 h infiltration of MAI before addition of PbBr and 3 g L^{-1} diblock copolymer micelle concentration (green spectrum), dual-phase emission from a mixture of particles with 24 h infiltration and 12 g L^{-1} micelle concentration (brown spectrum), and dominant red emission after 72 h infiltration of MAI, with 12 g L^{-1} micelle concentration (red spectrum). Note the large Stokes shift for the iodide-dominated solution. b) Schematic of STE formation due to coexistence of two halide ions. c–f) J - V characteristics of organic photovoltaic devices under a high-intensity UV light source. c) P3HT:PCBM and d) PTB7:PCBM organic solar cell before (black) and after (red) addition of bromine-dominant NPs (emission maxima at 505 nm). e) P3HT:PCBM and f) PTB7:PCBM organic solar cell before (black) and after (red) addition of iodine-dominant NPs (emission maxima at 706 nm). Each J - V image includes a reference performance without perovskite NP and the best performance of devices with perovskite NPs. Note that the device performance under UV light has not been optimized.

an increased concentration of reverse micelle nanoreactors, the particles have a $3\times$ higher density, with nearest-neighbor distance decreasing to 27.7 nm (see Figure S4b, Supporting Information). There is also the emergence of some smaller particles, of an average size of around 4.7 ± 0.9 nm; however, most of the particles have a size of 8.0 ± 1.4 nm. A slight hypsochromic shift from 521 nm for pure MAPbBr₃ phase to 518 nm is observed in Figure 4a (brown spectrum) for the higher-polymer concentration samples, which might be attributed to the change of size of the NPs due to the increased density of the nanoreactors.^[65] Note also that the iodide-dominant emission peak was broad (FWHM of 73.12 nm) compared with pure MAPbI₃ (FWHM of 50.9 nm) formation without PbBr₃; possible reasons could also be a difference in NP sizes, with some smaller particles emerging or the existence of mixed-halide structures causing a blueshift in the MAPbI₃ emission.^[66,67]

The formation of both iodide and bromide perovskite simultaneously suggests an uneven loading of the iodide ion into the micelles after 24 h for this larger amount of available nanoreactors. Cores where an excess of iodide was loaded resulted in MAPbI₃-dominant particles while those with a scarcity of iodide led to MAPbBr₃-dominant particles upon the introduction of the second precursor.

Therefore, we increased the infiltration time by a factor of three before the addition of the second precursor to allow for maximum loading of MAI to the core. Previously, we established that infiltration can be quantified by an increasing Young's modulus as measured by quantitative nanomechanical mapping (QNM) across the micelle core compared with an unloaded nanoreactor.^[13,68] As shown in Figure S6 (Supporting Information) the infiltration increases with stirring time and plateaus after 50 h. This plateau is thought to be due to the maximum salt infiltration and interaction with the polymer.^[68] To ensure maximum infiltration, the second precursor PbBr₃, slightly in excess of the MAI, was added after 72 h stirring. As can be seen from the PL emission spectrum in Figure 4a (red spectrum), the MAPbI₃-like emission peak dominates the spectrum. The MAPbBr₃-like emission is almost not visible, with a broad enhancement observed between 470 and 540 nm. This spectrum is similar to that observed in Figure 1e for conversion of fully formed MAPI with Br salt addition (see Figure S7, Supporting Information). This suggests that a higher number of MAPbI₃ (iodide dominant) NPs and a lower number of MAPbBr₃ (bromide dominant) NPs were synthesized or that formed MAPbI₃ were incompletely substituted with Br. This is likely due to an excess of iodide ions in the core, from the longer loading time beyond the maximum infiltration. Due to the very strong affinity between Pb and I in 2VP (0.17 eV),^[14] lead (Pb) would be expected to infiltrate first, followed by the infiltration of Br⁻. In the excess of iodide, potentially free iodine is available in the core, not interacting with the polymer, resulting in the preferential formation of MAPbI₃ with respect to MAPbBr₃. As shown in Figure 1e for conventionally produced MAPbI₃, once a stable MAPbI₃ NP is formed inside a nanoreactor, all the iodine cannot be replaced fully by halide substitution.

The loading results suggests that with a lower concentration of MAI, and shorter loading times, a scarcity of iodide ions in the core results in a MAPbBr₃-dominant perovskite cage. The MAPbBr₃ NPs formed using the unconventional route are not

halide-substituted MAPbI₃; they seem to be formed through the infiltration of Br⁻ ions which occupy the halide sites, causing perovskite (MAPbBr₃) formation and stabilizing the symmetry of the perovskite cage. Subsequently, by changing parameters that affects the amount of iodide in the core, we can synthesize stable iodide- or bromide-dominant solutions.

The presence of both iodide- and bromide-dominant NPs in a single solution showcases the phase stability and shielding effect resulting from the use of micelle templates. Neither NP degrades into an intermediate phase, unlike that observed for ligand-assisted systems.^[11] Interestingly due to the mixture of phases in the NPs, our dual-phase system shows an extremely large Stokes shift, with over 150 nm gap between the emission and absorption spectra.

In general, the Stokes shift is a spectral difference between the maximum peaks of absorption and emission spectra in the same transition. In some materials such as semiconductor quantum dots (QDs)^[69] and perovskites,^[11] it is hard to determine the maximum absorption peak in the UV-vis spectra. In addition, for broad absorption such as that observed for perovskites generally, the possibility of self-absorption is high, and the pure absorption of a downconverter could be low even if the universal Stokes shift is high. In this case, using the generalized concept of Stokes shift can result in an error in determining the validity of the downconverter. Thus, it is common to use the gap from the absorption edge to the highest peak of the photoluminescent region as the definition of the Stokes shift, as a criterion to judge whether the downconverter would be efficient taking into account the pure absorption of the downconverter.^[11,69,70]

In our case, in the dual-phase solution in which MAI was allowed for maximum infiltration followed by PbBr₃ (red spectrum, Figure 4a), the Stokes shift is caused by the formation of mixed-halide octahedrons due to both iodide and bromide incorporation. Merging of both iodide and bromide creates STE,^[71,72] which is an established mechanism for Stokes shifts in 0D perovskites. STE refers to the trapped-bound exciton that acts as a polaron due to photoexcitation in an altered lattice because of the presence of mixed halides.^[73] Once this low-energy state is developed because of multiple halides, the electrons are first excited to the high-energy excited state and consequently, shifted to the lower-excited energy state,^[74,75] resulting in broad emission with a large Stokes shift. This is exactly the case shown in Figure 4a, where the red spectrum has a broad emission (FWHM of 73.12 nm) far from the absorption edge. A schematic diagram of the band splitting indicating the states is shown in Figure 4b. This STE mechanism is also supported by the slight bathochromic shift in the absorption spectrum edge, which is slightly redshifted ($\Delta\lambda = 35$ nm) compared with the absorption edge of pure MAPbBr₃ and blueshifted ($\Delta\lambda = -175$ nm) compared with that of pure MAPbI₃ with a bandgap of 2.14 eV, (see Figure S3, Supporting Information, (red spectrum) for the Tauc plot). This behavior was also observed for the emission maximas, which were higher than pure MAPbBr₃ but lower than pure MAPbI₃, displayed in Figure 4a (red spectrum). As shown schematically in Figure 4b, a small amount of energy is released when the excited electron is shifted from a higher-energy excited state to a lower-energy state followed by a transition to the ground state, due to mixed-halide octahedrons, generating the observed Stokes shift.

Using this principle of establishing the Stokes shift from the absorption edge to the highest emission peak, the synthesized NPs were used for downconversion and UV filtering in OPVs. Though there has been some interest in using metal halide perovskites for downconversion,^[76,77] typically perovskites have a small Stokes shift compared with other common downconversion materials such as organic dyes.^[78] This typically results in significant parasitic absorption (PA) by the perovskite downconverter material. In such a case, device performance may actually decrease as the emitted visible light could be absorbed by the downconversion materials before going into and being used in the active layer.^[70] As a rule of thumb, a Stokes shift of above 100 nm is required for increased performance and zero reabsorption by downconverters. As we observed a Stokes shift of 150 nm with the iodine-dominant NP system, we believed this system could be a suitable downconverter. To show the efficacy of the NPs, different active materials were used to match the absorption of the device with the emission of NPs. P3HT:PCBM shows an absorbance region between 350 and 620 nm^[79] with optimal absorption (as defined by the highest absorption coefficient or the highest measured external quantum efficiency, as shown in Table S3, Supporting Information) between 500 and 620 nm. As such, it would be expected to show enhancement with bromine-dominant (green-emitting) NPs under UV illumination but none with the iodine-dominant (red-emitting) NPs. PTB7:PCBM, with optimal absorbance between 600 and 700 nm,^[80] on the other hand, should be enhanced with the iodine-dominant (red-emitting) NPs. As shown in Figure 4c–f, this was the behavior observed for organic photovoltaics (OPVs) under UV illumination conditions. Figure 4c shows the current density–voltage characterization curves of the P3HT:PCBM device under UV illumination. The black and red curve shows the results before and after the deposition of green-emitting NPs (brown curve in Figure 4c), respectively. The increase in short-circuit current indicates that the bromide-dominant ($\lambda_{\text{major_emission}} = 508$ nm) NPs acted as downconverters for P3HT:PCBM devices. The same dual-phase solution when used with PTB7:PCBM showed only a minor increase in the short-circuit current. This improvement could be attributed to the presence of some red emission ($\lambda_{\text{minor_emission}} = 704$ nm), which can be seen in the emission spectrum as well, or due to the weaker absorption of PTB7 around 500 nm (see Table S3, Supporting Information). The improvement can be seen in Figure 4d, which is negligible when compared with the P3HT:PCBM device with the same NPs.

For the iodine-dominant red-emitting dual-phase NPs ($\lambda_{\text{major_emission}} = 710$ nm, $\lambda_{\text{minor_emission}} = 515$ nm), the P3HT:PCBM device showed no obvious changes in the J – V characteristics (as shown in Figure 4e), demonstrating that there was no significant downconversion observed. This is likely a result of the absorption region of the device (from 350 to 620 nm) not overlapping with the major emission wavelength of the red emitters (≈ 700 nm). On the other hand, when the same red-emitting NPs were applied to the PTB7:PCBM device, a huge increase in the short circuit was observed. This confirms that the red-emitting NPs absorb in the UV region and emit mainly in the red wavelengths, making them excellent candidates as active UV filters. The drastic difference between the improved short circuit current

shown in Figure 4f for PTB7 devices with the red-emitting particles compared with the more limited improvement for P3HT with the green-emitting particles also confirms the extremely large Stokes shift in the case of red particles. In the green-emitting particles, where there is a negligible Stokes shift, PA might be limiting the efficiency of downconversion. Our dual-phase red-emitting system generates one of the largest Stokes shifts so far reported for a perovskite system, making them excellent candidates for downconversion for UV-sensitive materials.

3. Conclusion

By taking advantage of the slower reaction kinetics resulting from the use of diblock copolymer micelles, we have used an unconventional approach, that is, mixing MAI and PbBr₃ to produce monodispersed, uniform, stable, and highly luminescent MAPbBr₃ NPs, as well as coemitting solutions made up of both MAPbBr₃ and MAPbI₃ simultaneously. The unconventionally formed MAPbBr₃ NPs are not halide-substituted MAPbI₃; they are formed through the infiltration of Br[−] ions which then occupy the halide sites, stabilizing the symmetry of the perovskite cage. Varying the concentration of iodine, by increasing infiltration time, amount of precursors, and concentration of nanoreactors in the presence of both iodine and bromine ions, we were also able to synthesize both perovskite NPs in a single solution with different concentrations of MAPbI₃-dominant and MAPbBr₃-dominant NPs. It was even possible to extend this to other A-site organic cations, such as FAI, to form FAPbBr₃ and FAPbI₃ mixtures and pure phases. The micelle environment provided shielding for the perovskite, leading to phase stability, allowing the coexistence of multiple simultaneously emitting perovskite phases, and in addition to providing environmental stability. The presence of both bromine- and iodine-dominant particles resulted in the emergence of a large Stokes shift for the dual-phase systems due to self-trapped exciton formation. This allowed such particles to be used as efficient downconverters for OPVs without significant reabsorption. Downconversion for both P3HT:PCBM and PTB7:PCBM bulk heterojunction devices was obtained from the same precursors purely by changing the synthesis conditions during NP formation. Exploiting the phase-stabilizing effect of the micelles, the reaction kinetics of perovskite formation can be tuned to allow for the various halide substitutions, opening up new avenues for coexisting perovskite phases for photovoltaic and light-emitting applications.

4. Experimental Section

Perovskite Precursor Solution Preparation: 0.5 M precursor solutions were made by adding organic salts (methylammonium iodide (MAI), formadium iodide (FAI), methylammonium bromide), Sigma-Aldrich) to isopropanol (IPA) (Caledon, reagent grade), and the inorganic salts (lead(II) iodide (PbI₂, Alfa Aesar, 99.9985%) and lead(II) bromide (PbBr₂, Sigma-Aldrich 99.99%) to *N,N*-dimethylformamide (DMF) (Sigma Aldrich, 99.8%).

Nanoparticles Synthesis: Reverse micelles were prepared by dissolving poly(styrene-*b*-2-vinyl pyridine) diblock copolymers (Polymer Source) (molecular weight: 75.0-*b*-66.5 or 28.0-*b*-36.0 kDa), in reagent-grade non-polar solvent *o*-xylene, with concentration of 3 g L^{−1} under continuous stirring. For some experiments, the polymer-to-solvent ratio was changed to

12 g L⁻¹. After confirmation of reverse micelles formation by AFM, precursor salts and reactants were added to the reverse micelles solutions, with a time interval of 24 h, to allow thorough infiltration of each precursor. Pure methylammonium lead bromide (MAPbBr₃) was formed by mixing 0.5 M precursor solutions of MAI in IPA and PbBr₃ in DMF sequentially in the micelle solution. To obtain mixed MAPbI₃/MAPbBr₃ phases, conditions and parameters were changed slightly. For a mixed-phase solution with more MAPbBr₃ and less MAPbI₃, 12 g L⁻¹ of the diblock copolymer was dissolved in *o*-xylene. After the formation of the nanoreactors, 10 µL of MAI was added to the solution to penetrate into the core of the nanoreactor, followed by the addition of 10 µL of PbBr₃. For a solution with more MAPbI₃ and less MAPbBr₃, 10 µL of MAI in IPA was added to the 12 g L⁻¹ reverse micelle solution and was left to stir for 72 h to allow maximum infiltration, followed by the addition of PbBr₃. The final loaded reverse micelle solutions were centrifuged to clear out the unloaded excess salt and stirred further to prevent coagulation. 4 µL of solution was spin coated on silicon (1 × 1) cm slab for AFM characterization.

For LARP synthesis, 12.5 mg (0.034 mmol, 1 equiv.) of PbBr₃ was weighed into a vial to which 6.0 mg (0.37 mmol, 1.1 equiv.) of MAI or MABr was added. Furthermore, oleic acid (0.320 mmol, 9.4 equiv.) along with oleylamine (0.027 mmol, 0.8 equiv.) were added to the vial. DMF was added to the mixture of precursors to reach 1.25 mL. To precipitate the NPs, 12.5 mL of previously dried toluene (molecular sieve, 3 Å) was cooled in an ice bath to ≈5 °C while stirring, and 75 µL from the mixed precursors vial was added to the chilled toluene and stirred for 2 min. To deposit the synthesized NPs on a substrate, a thoroughly cleaned glass slide (0.9 × 0.9 cm) was plasma treated and placed at the bottom of a centrifugation tube. The colloidal solution along with 37 mL EtOAc was gently added to the centrifugation tube, and centrifuged at 5000 rpm for 5 min, resulting in the deposition of the NPs on the glass slide. Using a Pasteur pipette, the supernatant was carefully removed, and the film was placed in a vial and dried in toluene atmosphere. After the NP thin film dried, it was placed on a hot plate at 120 °C. As soon as the colour change was visible (≈10 s), the film was removed and stored in a glass vial under ambient conditions.

Organic Solar Cell Fabrication: The organic solar cells were based on a convention standard structure of ITO/PEDOT:PSS/bulk heterojunction/aluminum (Al). Active layers consisted of poly(3-hexylthiophene) (P3HT) or poly[[4,8-bis[(2-ethylhexyl)oxy]benzo[1,2-b:4,5-b']dithiophene-2,6-diyl][3-fluoro-2-[(2-ethylhexyl)carbonyl]thieno[3,4-b]thiophenediyl]] (PTB7) blended with [6,6]-phenyl C61-butyric acid methylester (PCBM).

The ITO substrates were cleaned by acetone and 2-propanol (IPA) for 15 min respectively in an ultrasonic cleaner to obtain a dust-free substrate and were etched for 5 min in oxygen plasma to remove residual chemicals. Then, poly(3,4-ethylenedioxythiophene) polystyrene sulfonate (PEDOT:PSS) mixed with 50% of IPA was spin coated on ITO at 3000 rpm for 30 s and annealed at 150 °C for 10 min in the glovebox (inert atmosphere). For PTB7:PCBM, 25 mg mL⁻¹ PTB7:PCBM (weight ratio: 1:1.5) in chlorobenzene was deposited on the top of PEDOT:PSS subsequently at 2000 rpm for 30 s before drying the substrate overnight. Regarding P3HT:PCBM deposition, 15 mg mL⁻¹ P3HT:PCBM (weight ratio: 1:1) in chlorobenzene was used, followed by substrate annealing at 120 °C for 10 min. After that, Al electrodes were deposited by thermal evaporation with a mask to limit the active area in 0.06 cm² under low pressure of 10⁻⁶ mbar. The encapsulated device was postannealed at 150 °C for 10 min in ambient environment to enhance the self-conjugation of the organic blend. To investigate the UV conversion of perovskite NPs, a small amount of perovskite was layered on the bottom of ITO-coated glass by spin coating at 2000 rpm for 20 s. The characterization of solar cells was under a UV light source with a strong intensity at around 395 nm in ambient environment. Note that under UV illumination, the device with perovskites was measured at first to highlight the UV blocking of perovskites; then, the perovskite NPs were removed before the device was measured again under the same illumination conditions.

Characterization: AFM images were collected using an Asylum MFP-3D instrument (Oxford Instruments Asylum Research) in the alternating current (AC) mode under ambient environment. AFM probes (Nanotools, EBD-FMR) with spring constant of 2.8 N m⁻¹ and resonant frequency

at 75 kHz were engaged in tapping mode for topography scan. WS × M 5.0 was used for AFM image processing. All AFM samples were prepared by spin coating 4 µL of solution at 2000 rpm for 45 s on (1 × 1) cm silicon slab.

PL measurements were performed using a 405 nm diode laser with laser power in the range of 11 mW (spot diameter: 1–2 mm). The sample emission was collected with a lens and guided to the detection unit with an optical fiber. A long-pass filter (550 nm) removed the excitation light before the collected radiation was fed into a monochromator (Andor, Shamrock 303i, grating 500 nm blaze, 150 lines mm⁻¹) and detected with an intensified charge-coupled device (Andor, iStar A-DH320T-18U-73). The sample was introduced to the laser with an exposure time of 0.0237 s and a slit opening of 50 µm. The detection range was from 500 to 900 nm. The measurement was taken in the dark to prevent stray light.

UV–vis spectra measurements were performed to characterize the optical properties of the materials using a Lambda 35 UV-Visible spectrometer (PerkinElmer). The samples were prepared at concentrations 0.1 mg mL⁻¹, using *o*-xylene as dispersant, measured in a 1 × 1 cm quartz cuvette.

Supporting Information

Supporting Information is available from the Wiley Online Library or from the author.

Acknowledgements

The authors thank the McMaster Manufacturing Research Institute (MMRI), Centre for Advanced Light Microscopy (CALM) and the BioInterfaces Institute, for access to the atomic force microscopy for measurements, the Canadian Centre for Electron Microscopy (CCEM) for HRTEM measurements, and McMaster X-Ray Diffraction Facility (MAX) for XRD. A.T. acknowledges financial support from the Ontario Ministry of Research and Innovation (Early Researcher Award, ER15-11-123), the Natural Science and Engineering Research Council of Canada (Discovery Grant, RGPIN-2019-05994), and Satellite Canada Innovation Network (HTSN-611, and HTSN-621), as well as the Austrian Science Foundation FWF within the Wittgenstein Prize for N.S.S.

Conflict of Interest

The authors declare no conflict of interest.

Data Availability Statement

The data that support the findings of this study are available from the corresponding author upon reasonable request.

Keywords

diblock copolymers, downconversion, micellar shielding, P3HT, perovskites, PTB7, stability

Received: January 21, 2022

Revised: June 10, 2022

Published online:

- [1] I. Dursun, C. Shen, M. R. Parida, J. Pan, S. P. Sarmah, D. Priante, N. Alyami, J. Liu, M. I. Saidaminov, M. S. Alias, A. L. Abdelhady, T. K. Ng, O. F. Mohammed, B. S. Ooi, O. M. Bakr, *ACS Photonics* **2016**, *3*, 1150.

- [2] S. W. Eaton, M. Lai, N. A. Gibson, A. B. Wong, L. Dou, J. Ma, L. W. Wang, S. R. Leone, P. Yang, *Proc. Natl. Acad. Sci.* **2016**, *113*, 1993.
- [3] S. Yakunin, L. Protesescu, F. Krieg, M. I. Bodnarchuk, G. Nedelcu, M. Humer, G. D. Luca, M. Fiebig, W. Heiss, M. V. Kovalenko, *Nat. Commun.* **2015**, *6*, 8056.
- [4] H. J. Snaith, *J. Phys. Chem. Lett.* **2013**, *4*, 3623.
- [5] H. Zhang, H. Xu, X. Ji, J. Liang, *Energy Fuels* **2020**, *34*, 6624.
- [6] J. P. Correa-Baena, M. Saliba, T. Buonassisi, M. Grätzel, A. Abate, *Science* **2017**, *358*, 739.
- [7] Z. Liu, M. Hu, J. Du, T. Shi, Z. Wang, Z. Zhang, Z. Liu, M. Hu, J. Du, T. Shi, Z. Wang, Z. Zhang, Z. Hu, Z. Zhan, K. Chen, W. Liu, J. Tang, H. Zhang, Y. Leng, R. Li, *ACS Nano* **2021**, *15*, 6900.
- [8] S.-H. Turren-Cruz, A. Hagfeldt, M. Saliba, *Science* **2018**, *362*, 449.
- [9] X. He, P. Guo, J. Wu, Y. Tu, Z. Lan, J. Lin, M. Huang, *Sol. Energy* **2017**, *157*, 853.
- [10] Z. Li, M. Yang, J. S. Park, S. H. Wei, J. J. Berry, K. Zhu, *Chem. Mater.* **2016**, *28*, 284.
- [11] G. Nedelcu, L. Protesescu, S. Yakunin, M. I. Bodnarchuk, M. J. Grotevent, M. V. Kovalenko, *Nano Lett.* **2015**, *15*, 5635.
- [12] L. Protesescu, S. Yakunin, M. I. Bodnarchuk, F. Krieg, R. Caputo, C. H. Hendon, R. X. Yang, A. Walsh, M. V. Kovalenko, *Nano Lett.* **2015**, *15*, 3692.
- [13] L. S. Hui, C. Beswick, A. Getachew, H. Heilbrunner, K. Liang, G. Hanta, R. Arbi, M. Munir, H. Dawood, N. I. Goktas, R. LaPierre, M. C. Scharber, N. S. Sariciftci, A. Turak *ACS Appl. Nano Mater.* **2019**, *2*, 4121.
- [14] S. Hou, Y. Guo, Y. Tang, Q. Quan, *ACS Appl. Mater. Interfaces* **2017**, *9*, 417.
- [15] Y. He, Y. J. Yoon, Y. W. Harn, G. V. Biesold-McGee, S. Liang, C. H. Lin, V. V. Tsukruk, N. Thadhani, Z. Kang, Z. Lin, *Sci. Adv.* **2019**, *5*, eaax4424.
- [16] A. Pan, L. Yan, X. Ma, Y. Wu, Y. Zhang, G. Zhou, H. Ling, *J. Alloys* **2020**, *156*, 102.
- [17] K. Wang, L. Zheng, T. Zhu, L. Liu, M. L. Becker, X. Gong, *Nano Energy* **2020**, *67*, 229.
- [18] E. Ercan, P. C. Tsai, J. Y. Chen, J. Y. Lam, L. C. Hsu, C. C. Chueh, W.-C. Chen, *ACS Appl. Mater. Interfaces* **2019**, *11*, 615.
- [19] Y. Zhang, Y. Zhao, D. Wu, J. Xue, Y. Qiu, M. Liao, Q. Pei, M. S. Goorsky, X. He, *Adv. Mater.* **2019**, *31*, 1.
- [20] K. Liang, L. Shu Hui, A. Turak, *Nanoscale* **2019**, *11*, 9076.
- [21] A. Pan, M. J. Jurow, F. Qiu, J. Yang, B. Ren, J. J. Urban, L. He, Y. Liu, *Nano Lett.* **2017**, *17*, 6759.
- [22] S. Mollick, T. N. Mandal, A. Jana, S. Fajal, A. V. Desai, S. K. Ghosh, *ACS Appl. Nano Mater.* **2019**, *2*, 1333.
- [23] H. Huang, B. Chen, Z. Wang, T. Fu Hung, A. S. Sussha, H. Zhong, A. L. Rogach, *Chem. Sci.* **2016**, *7*, 5699.
- [24] F. Liu, C. Ding, Y. Zhang, T. S. Ripolles, T. Kamisaka, T. Toyoda, S. Hayase, T. Minemoto, K. Yoshino, S. Dai, M. Yanagida, H. Noguchi, Q. Shen, *J. Am. Chem. Soc.* **2017**, *139*, 16.
- [25] Z. Hu, Z. Liu, Z. Zhan, T. Shi, J. Du, X. Tang, Y. Leng, *Adv. Photonics* **2021**, *3*, 034 002.
- [26] G. Evano, A. Nitelet, P. Thilmann, D. F. Dewez, *Front. Chem.* **2018**, *6*, 114.
- [27] Y. H. Kim, H. Cho, T. W. Lee, *Proc. Natl. Acad. Sci.* **2016**, *113*, 11 694.
- [28] Y.-H. Kim, H. Cho, J. H. Heo, T.-S. Kim, N. S. Myoung, C.-L. Lee, S. H. Im, T.-W. Lee, *Adv. Mater.* **2015**, *27*, 1248.
- [29] D. M. Jang, K. Park, D. H. Kim, J. Park, F. Shojaei, H. S. Kang, J.-P. Ahn, J. W. Lee, J. K. Song, *Nano Lett.* **2015**, *15*, 5191.
- [30] Z. Yi, N. H. Ladi, X. Shai, H. Li, Y. Shen, M. Wang, *Nanoscale Adv.* **2019**, *1*, 1276.
- [31] V. A. Hintermayr, A. F. Richter, F. Ehrat, M. Döblinger, W. Vanderlinden, J. A. Sichert, Y. Tong, L. Polavarapu, J. Feldmann, A. S. Urban, *Adv. Mater.* **2016**, *28*, 9478.
- [32] L. C. Schmidt, A. Pertegás, S. González-Carrero, O. Malinkiewicz, S. Agouram, G. M. Espallargas, H. J. Bolink, R. E. Galian, J. Pérez-Prieto, *J. Am. Chem. Soc.* **2014**, *136*, 850.
- [33] M. Chauhan, Y. Zhong, K. Schötz, B. Tripathi, A. Köhler, S. Huettnner, F. Panzer, *J. Mater. Chem. A* **2020**, *8*, 5086.
- [34] H. Huang, A. S. Sussha, S. V. Kershaw, T. F. Hung, A. L. Rogach, *Adv. Sci.* **2015**, *2*, 1.
- [35] H. H. Ma, M. Imran, Z. Dang, Z. Hu, *Crystals* **2018**, *8*, 182.
- [36] V. S. Chirvony, J. P. Martínez-Pastor, *J. Phys. Chem. Lett.* **2018**, *9*, 4955.
- [37] R. Arbi, A. Ibrahim, L. Goldring-Vandergest, K. Liang, G. Hanta, L. S. Hui, A. Turak, *Nano Sel.* **2021**, *2*, 2419.
- [38] L. S. Hui, M. Munir, A. Vuong, M. Hilke, V. Wong, G. Fanchini, M. C. Scharber, N. S. Sariciftci, A. Turak, *ACS Appl. Mater. Interfaces* **2020**, *12*, 46.
- [39] F. Zhang, H. Zhong, C. Chen, X. Wu, X. Hu, H. Huang, J. Han, B. Zou, Y. Dong, *ACS Nano* **2015**, *9*, 4533.
- [40] M. Imran, F. Di Stasio, Z. Dang, C. Canale, A. H. Khan, J. Shamsi, R. Brescia, M. Prato, L. Manna, *Chem. Mater.* **2016**, *28*, 6450.
- [41] A. Pisanu, P. Quadrelli, L. Malavasi, *RSC Adv.* **2019**, *9*, 13 263.
- [42] H. Jiang, S. Cui, Y. Chen, H. Zhong, *Nano Sel.* **2021**.
- [43] Y. J. Yoon, K. T. Lee, T. K. Lee, S. H. Kim, Y. S. Shin, B. Walker, S. Y. Park, J. Heo, J. Lee, S. K. Kwak, G.-H. Kim, J. Y. Kim, *Joule* **2018**, *2*, 2105.
- [44] W. J. Shin, J. Y. Kim, G. Cho, J. S. Lee, *J. Mater. Chem.* **2009**, *19*, 7322.
- [45] Z. Zhang, M. M. Rahman, C. Abetz, B. Bajer, J. Wang, V. Abetz, *Macromol. Rapid Commun.* **2019**, *40*, 1800729.
- [46] M. Bumstead, K. Liang, G. Hanta, L. S. Hui, A. Turak, *Sci. Rep.* **2018**, *8*, 1554.
- [47] A. Jaffe, Y. Lin, C. M. Beavers, J. Voss, W. L. Mao, H. I. Karunadasa, *ACS Cent. Sci.* **2016**, *2*, 201.
- [48] M. R. Libera, R. F. Egerton, *Polym. Rev.* **2010**, *50*, 321.
- [49] G. G. Aloisi, G. Beggiato, U. Mazzucato, *Trans. Faraday Soc.* **1970**, *66*, 3075.
- [50] C. F. Merlevede, G. Maes, *Adv. Mol. Relax. Interact. Process.* **1980**, *16*, 111.
- [51] B. Brunetti, C. Cavallo, A. Ciccio, G. Gigli, A. Latini, *Sci. Rep.* **2016**, *6*, 896.
- [52] G. P. Nagabhushana, R. Shivaramaiah, A. Navrotsky, *Proc. Natl. Acad. Sci.* **2016**, *113*, 7717.
- [53] I. L. Ivanov, A. S. Steparuk, M. S. Bolyachkina, D. S. Tsvetkov, A. P. Safronov, A. Y. Zuev, *J. Chem. Thermodyn.* **2018**, *116*, 253.
- [54] D. T. Moore, H. Sai, K. W. Tan, D. M. Smligies, W. Zhang, H. J. Snaith, U. Wiesner, L. A. Estroff, *J. Am. Chem. Soc.* **2015**, *137*, 2350.
- [55] M. A. Uddin, J. D. Glover, S. M. Park, J. T. Pham, K. R. Graham, *Chem. Mater.* **2020**, *32*, 5217.
- [56] Y. Lei, L. Gu, X. Yang, L. Zhang, Y. Gao, J. Li, Z. Zheng, *J. Alloys Compd.* **2018**, *766*, 933.
- [57] C. Liu, Y. B. Cheng, Z. Ge, *Chem. Soc. Rev.* **2020**, *49*, 1653.
- [58] J. Qiu, Y. Zheng, Y. Xia, L. Chao, Y. Chen, W. Huang, *Adv. Funct. Mater.* **2019**, *29*, 1806831.
- [59] A. Ciccio, A. Latini, *J. Phys. Chem. Lett.* **2018**, *9*, 3756.
- [60] S. Aharon, L. Etgar, *Nano Lett.* **2016**, *16*, 3230.
- [61] I. Levchuk, P. Herre, M. Brandl, A. Osvet, R. Hock, W. Peukert, P. Schweizer, E. Spiecker, M. Batentschuk, C. J. Brabec, *Chem. Commun.* **2017**, *53*, 244.
- [62] C. Guhrens, A. Benad, C. Ziegler, D. Haubold, N. Gaponik, A. Eychmüller, *Chem. Mater.* **2016**, *28*, 9033.
- [63] V. A. Hintermayr, C. Lampe, M. Löw, J. Roemer, W. Vanderlinden, M. Gramlich, A. X. Böhm, C. Sattler, B. Nickel, T. Lohmüller, A. S. Urban, *Nano Lett.* **2019**, *19*, 4928.
- [64] S. S. Kulthe, Y. M. Choudhari, N. N. Inamdar, V. Mourya, *Des. Monomers Polym.* **2012**, *15* 465.

- [65] D. Di, K. P. Musselman, G. Li, A. Sadhanala, Y. Ievskaya, Q. Song, Z.-K. Tan, M. L. Lai, J. L. MacManus-Driscoll, N. C. Greenham, R. H. Friend, *J. Phys. Chem. Lett.* **2015**, *6*, 446.
- [66] Y.-H. Kim, C. Wolf, Y.-T. Kim, H. Cho, W. Kwon, S. Do, A. Sadhanala, C. G. Park, S.-W. Rhee, S. H. Im, R. H. Friend, T.-W. Lee, *ACS Nano* **2017**, *11*, 6586.
- [67] D. N. Minh, J. Kim, J. Hyon, J. H. Sim, H. H. Sowlih, C. Seo, J. Nam, S. Eom, S. Suk, S. Lee, E. Kim, Y. Kang, *Chem. Mater.* **2017**, *29*, 5713.
- [68] G. Hanta, *Stability, And Nanoparticle Spatial Distribution*, Master of Applied Science, McMaster University, Hamilton, ON **2019**.
- [69] K. Wu, H. Li, V. I. Klimov, *Nat. Photon* **2018**, *12*, 105.
- [70] N. Bristow, Doctoral, Bangor University UK, **2017**.
- [71] C. Zhou, H. Lin, Q. He, L. Xu, M. Worku, M. Chaaban, S. Lee, X. Shi, M.-H. Du, B. Ma, *Mater. Sci. Eng. R. Rep.* **2019**, *137*, 38.
- [72] M. D. Smith, B. A. Connor, H. I. Karunadasa, *Chem. Rev.* **2019**, *119*, 3104.
- [73] D. Han, H. Shi, W. Ming, C. Zhou, B. Ma, B. Saparov, Y.-Z. Ma, S. Chen, M.-H. Du, *J. Mater. Chem. C* **2018**, *6*, 6398.
- [74] Z. Yuan, C. Zhou, Y. Tian, Y. Shu, J. Messier, J. C. Wang, L. J. van de Burgt, K. Kountouriotis, Y. Xin, E. Holt, K. Schanze, R. Clark, T. Siegrist, B. Ma, *Nat. Commun.* **2017**, *8*, 14051.
- [75] T. Hu, M. D. Smith, E. R. Dohner, M.-J. Sher, X. Wu, M. T. Trinh, A. Fisher, J. Corbett, X.-Y. Zhu, H. I. Karunadasa, A. M. Lindenberg, *J. Phys. Chem. Lett.* **2016**, *7*, 2258.
- [76] L. Meng, X.-G. Wu, S. Ma, L. Shi, M. Zhang, L. Wang, Y. Chen, Q. Chen, H. Zhong, *Nanophotonics* **2020**, *9*, 93.
- [77] M. F. Abdelbar, M. El-Kemary, N. Fukata, *Nano Energy* **2020**, *105*, 163.
- [78] R. V. Fernandes, N. Bristow, V. Stoichkov, H. S. Anizelli, J. L. Duarte, E. Laureto, J. Kettle, *J. Phys. D: Appl. Phys.* **2016**, *50*, 025103.
- [79] P. R. Berger, M. Kim *J. Renew. Sustain. Energy* **2018**, *10*, 013508.
- [80] L. Lu, L. Yu *Adv. Mater.* **2014**, *26*, 4413.